
Distance determination of molecular clouds in the 1st quadrant of the Galactic plane using deep learning : I. Method and Results

Shinji FUJITA^{1,2}, Atsushi M. ITO³, Yusuke MIYAMOTO⁴, Yasutomo KAWANISHI⁵, Kazufumi TORII⁶, Yoshito SHIMAJIRI⁷, Atsushi NISHIMURA⁸, Kazuki TOKUDA^{9,6}, Toshikazu OHNISHI², Hiroyuki KANEKO^{10,6}, Tsuyoshi INOUE¹¹, Shunya TAKEKAWA¹², Mikito KOHNO^{13, 14}, Shota UEDA², Shimpei NISHIMOTO², Ryuki YONEDA², Kaoru NISHIKAWA¹⁴ and Daisuke YOSHIDA¹⁴

¹Institute of Astronomy, Graduate School of Science, The University of Tokyo, 2-21-1 Osawa, Mitaka, Tokyo 181-0015, Japan

²Department of Physical Science, Graduate School of Science, Osaka Prefecture University 1-1 Gakuen-cho, Naka-ku, Sakai, Osaka 599-8531, Japan

³National Institute for Fusion Science (NIFS), National Institutes of Natural Sciences (NINS) 322-6, Oroshi-cho, Toki, Gifu 509-5292, Japan

⁴Department of Electrical and Electronic Engineering, Faculty of Engineering, Fukui University of Technology, 3-6-1, Gakuen, Fukui, Fukui, 910-8505, Japan

⁵RIKEN Information R&D and Strategy Headquarters, 2-2-2 Hikaridai, Seika-cho, Soraku-gun, Kyoto 619-0288, Japan

⁶National Astronomical Observatory of Japan, National Institutes of Natural Sciences, 2-21-1 Osawa, Mitaka, Tokyo 181-8588, Japan

⁷Kyushu Kyoritsu University, Jiyugaoka 1-8, Yahatanishi-ku, Kitakyushu, Fukuoka, 807-8585 Japan

⁸Nobeyama Radio Observatory, National Astronomical Observatory of Japan, National Institutes of Natural Sciences, 462-2 Nobeyama, Minamimaki, Minamisaku, Nagano 384-1305, Japan

⁹Department of Earth and Planetary Sciences, Faculty of Sciences, Kyushu University,
Nishi-ku, Fukuoka 819-0395, Japan

¹⁰Graduate School of Education, Joetsu University of Education, 1, Yamayashiki-machi,
Joetsu, Niigata 943-8512, Japan

¹¹Department of Physics, Konan University, 8-9-1 Okamoto, Higashinada-ku, Kobe, Hyogo
658-8501, Japan

¹²Faculty of Engineering, Kanagawa University, 3-27-1 Rokkakubashi, Kanagawa-ku,
Yokohama, Kanagawa 221-8686, Japan

¹³Astronomy Section, Nagoya City Science Museum, 2-17-1 Sakae, Naka-ku, Nagoya, Aichi
460-0008, Japan

¹⁴Department of Astrophysics, Nagoya University, Furo-cho, Chikusa-ku, Nagoya, Aichi
464-8602, Japan

*E-mail: fujita.shinji@ioa.s.u-tokyo.ac.jp

Received ; Accepted

Abstract

Machine learning has been successfully applied in varied field but whether it is a viable tool for determining the distance to molecular clouds in the Galaxy is an open question. In the Galaxy, the kinematic distance is commonly employed to represent the distance to a molecular cloud. However, for the inner Galaxy, two different solutions, i.e., the “Near” solution and the “Far” solution, can be derived simultaneously. We attempt to construct a two-class (“Near” or “Far”) inference model using a convolutional neural network (CNN), which is a form of deep learning that can capture spatial features generally. In this study, we use the CO dataset in the 1st quadrant of the Galactic plane obtained with the Nobeyama 45-m radio telescope ($l = 62^\circ - 10^\circ$, $|b| < 1^\circ$). In the model, we apply the three-dimensional distribution (position–position–velocity) of the ^{12}CO ($J = 1 - 0$) emissions as the main input. To train the model, a dataset with “Near” or “Far” annotation was created from the HII region catalog of the infrared astronomy satellite WISE. Consequently, we construct a CNN model with a 76% accuracy rate on the training dataset. Using the proposed model, we determine the distance to the molecular clouds identified by the CLUMPFIND algorithm. We found that the mass of molecular clouds with a distance of < 8.15 kpc identified in the ^{12}CO data follows a power-law distribution with an index of approximately -2.3 in the mass range $M > 10^3 M_\odot$. In addition, the detailed molecular gas distribution of the Galaxy, as seen from the Galactic North pole, was determined.

1 Introduction

Stars are formed in molecular clouds. To better understand the initiation of star formation, investigating the physical properties of molecular clouds at various scales, from several hundred pc to sub pc, is vital. In addition, it is critical to study them throughout a galaxy because star formation is closely related to the structure and environment of galaxies. Recent advances in telescope technology have enabled wide-area CO surveys of many nearby galaxies [e.g., COMING (CO Multiline Imaging of Nearby Galaxies Muraoka et al. 2016; Sorai et al. 2019) and PHANGS (Physics at High Angular resolution in Nearby GalaxieS Rosolowsky et al. 2021; Leroy et al. 2021)]. The Atacama Large Millimeter/submillimeter Array (ALMA) has enabled the observation of M33 and the Large Magellanic Cloud/Small Magellanic Cloud with a spatial resolution of less than 1 pc, facilitating the study of the global structure of galaxies and the relationship between gas dynamics and star formation (e.g., Tokuda et al. 2020; Fukui et al. 2019). The spatial resolution of < 1 pc revealed filamentary structures of molecular clouds, the origin of which is currently under active discussion. The advances in telescope technology have also facilitated CO surveys of the Galaxy with higher angular resolution ($\sim 20''$ typically) and wide area (~ 100 ,degree² typically) [e.g., COHRS (CO High-Resolution Survey; Dempsey et al. 2013), FUGIN (FOREST Unbiased Galactic plane Imaging survey with the Nobeyama 45-m telescope; Umemoto et al. 2017)¹, SEDIGISM (Structure, Excitation, and Dynamics of the Inner Galactic Interstellar Medium; Schuller et al. 2021)]. The FUGIN observations toward the Galactic plane revealed the presence of many cloud–cloud collisions triggering high-mass star formation (e.g., Dewangan et al. 2020; Fujita et al. 2019; Fujita et al. 2021; Kohno et al. 2018; Nishimura et al. 2018; Torii et al. 2018). Furthermore, the dense gas mass fraction in the Galactic plane was measured with high angular resolution (Torii et al. 2019), although the analysis was limited to nearby tangential regions because of the uncertainty of the distance to molecular clouds.

For several decades, three-dimensional (3D) maps (or face-on maps) of the Galaxy have been a classic and fundamental topic. The most reliable data for distances and 3D maps of the Galaxy are observations of masers using very long baseline interferometry (VLBI) (e.g., Reid et al. 2014).

¹ <https://nro-fugin.github.io/>

These observations provide strong evidence of the existence of spiral arms in the Galaxy. However, the number of data points is limited, and determining the extent to which the molecular clouds are associated is difficult. The distance information of molecular clouds in the Galaxy is a significant parameter not only because of its mass and size, but also because it enables discussion of the Galaxy’s structure. The kinematic distance computed from the gas’s line-of-sight velocity and the Galaxy’s rotating velocity has been commonly employed; however, two different solutions, the “Near” solution and the “Far” solution, can be derived simultaneously for the gas in the inner solar system orbit (this is termed as the Near–Far problem). Several methods have been proposed to solve this problem and to determine the distance (e.g., Nakanishi & Sofue 2006; Riener et al. 2020; Mège et al. 2021). For example, assuming that the vertical distribution of H₂ gas follows the equation (sech² function obtained by treating it as an isothermal and self-gravitating system) in Spitzer (1942), Nakanishi & Sofue (2006) divided the CO data obtained with a CfA 1.2-m Millimeter-Wave Telescope (Dame et al. 2001) into “Near” and “Far” emissions; using this, they presented a 3D map of the molecular gas of the Galaxy. Riener et al. (2020) adopted a Bayesian approach (Reid et al. 2016; Reid et al. 2019) to derive the current best assessment of the Galactic distribution of ¹³CO from the Galactic Ring Survey (GRS) (Jackson et al. 2006).

Machine-learning techniques, particularly deep learning, are widely accepted as powerful tools in various fields. Deep learning has been particularly successful in the field of imaging, such as detection of disease in the medical field and typhoon in meteorology (e.g., Dabeer et al. 2019; Matsuoka et al. 2018). In astronomy, many studies have used machine learning, such as those on the morphological classification of galaxies and anomaly detection of signals (e.g., Bom et al. 2021; Villar et al. 2021). Ueda et al. (2020) attempted to identify infrared rings, which have been identified only by the human eye, using an object detection model based on a convolutional neural network (CNN; e.g., Schmidhuber 2014), which is a form of deep learning. They succeeded in developing a model that was comparable to human eyes.

In this paper (Paper I), our main motivation is to label all voxels of the CO data cube (position–position–velocity) as “Near” or “Far” using a CNN model. The kinematic distance to molecular clouds is then determined by combining the labels with the rotation parameter of the Galaxy; the physical properties of molecular clouds in the 1st quadrant of the Galactic plane can be observed with unprecedented high spatial resolution. In Section 2, we present the CO data, whereas in Section 3, we describe the CNN model. Next, in Section 4, we present cloud identification and distance determination. In Section 5, we show the ¹³CO face-on-view map of the Galaxy, whereas in Section 6, we highlight possible errors in distance estimation in this study. In the forthcoming paper (Paper II), we will discuss the physical properties of the molecular clouds, such as the dense gas mass fraction and

the Galactic structure. In this study, we assume that the rotation curve of the Galaxy is flat; moreover, we assume that the distance from the Sun to the Galactic center is 8.15 kpc, and adopt a rotation speed of 236 km s^{-1} (Reid et al. 2019).

2 Data

We used FUGIN ^{12}CO , ^{13}CO , and C^{18}O ($J = 1 - 0$) emission data obtained using the Nobeyama 45-m radio telescope ($l = 50^\circ - 10^\circ$, $|b| < 1^\circ$; Umemoto et al. 2017). See Umemoto et al. (2017) for details of the observations. We downloaded version 1.00, which fits the data cube from the archive site². We also used the ^{12}CO , ^{13}CO , and C^{18}O ($J = 1 - 0$) emission data obtained with the Nobeyama 45-m radio telescope ($l = 62^\circ - 50^\circ$, $|b| < 1^\circ$; Kohno et al. 2022; Nishimura et al. in prep.). These observations were conducted using a scan mode that is similar to FUGIN, and their effective spatial resolutions are $\sim 20''$. The velocity coverage ranges from -100 to $+200 \text{ km s}^{-1}$. In this study, the data cubes were spatially convoluted with $30''$ Gaussian (effective angular resolution of $\sim 36''.1$) to enhance the signal-to-noise ratio (S/N) and to remove the scanning effect. Figure 1 shows the peak brightness temperature map and the T_{rms} map of the three lines. The typical noise level (T_{rms}) is $1.0 - 1.5 \text{ K}$, $0.5 - 0.8 \text{ K}$, and $0.5 - 0.8 \text{ K}$ for ^{12}CO , ^{13}CO , and C^{18}O ($J = 1 - 0$) emissions in the main beam brightness temperature (T_{mb}) scale, respectively, although the T_{rms} map in Figure 1 is not uniform. The angular and velocity grid sizes were $8''.5$ and 0.65 km s^{-1} , respectively. The FITS cubes were created with a size of $2^\circ \times 2^\circ \times 300 \text{ km s}^{-1}$ ($848 \text{ pixels} \times 848 \text{ pixels} \times 462 \text{ channels}$) every 1° in the Galactic longitude (51 FITS cubes for each emission line).

² <http://jvo.nao.ac.jp/portal/nobeyama/fugin.do>

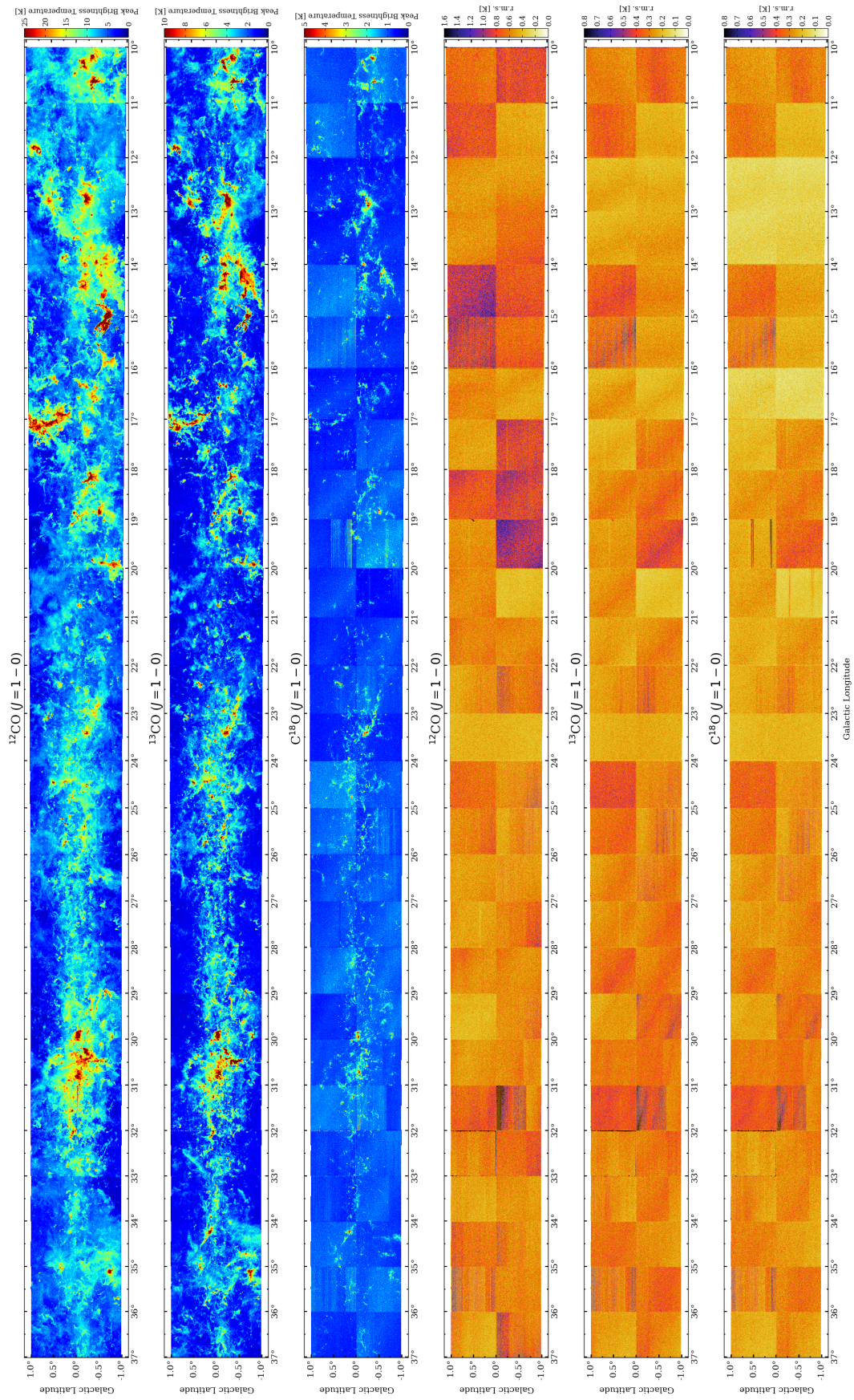


Fig. 1: Peak brightness temperature map and T_{rms} map of the ^{12}CO , ^{13}CO , and ^{13}CO ($J=1-0$) emission.

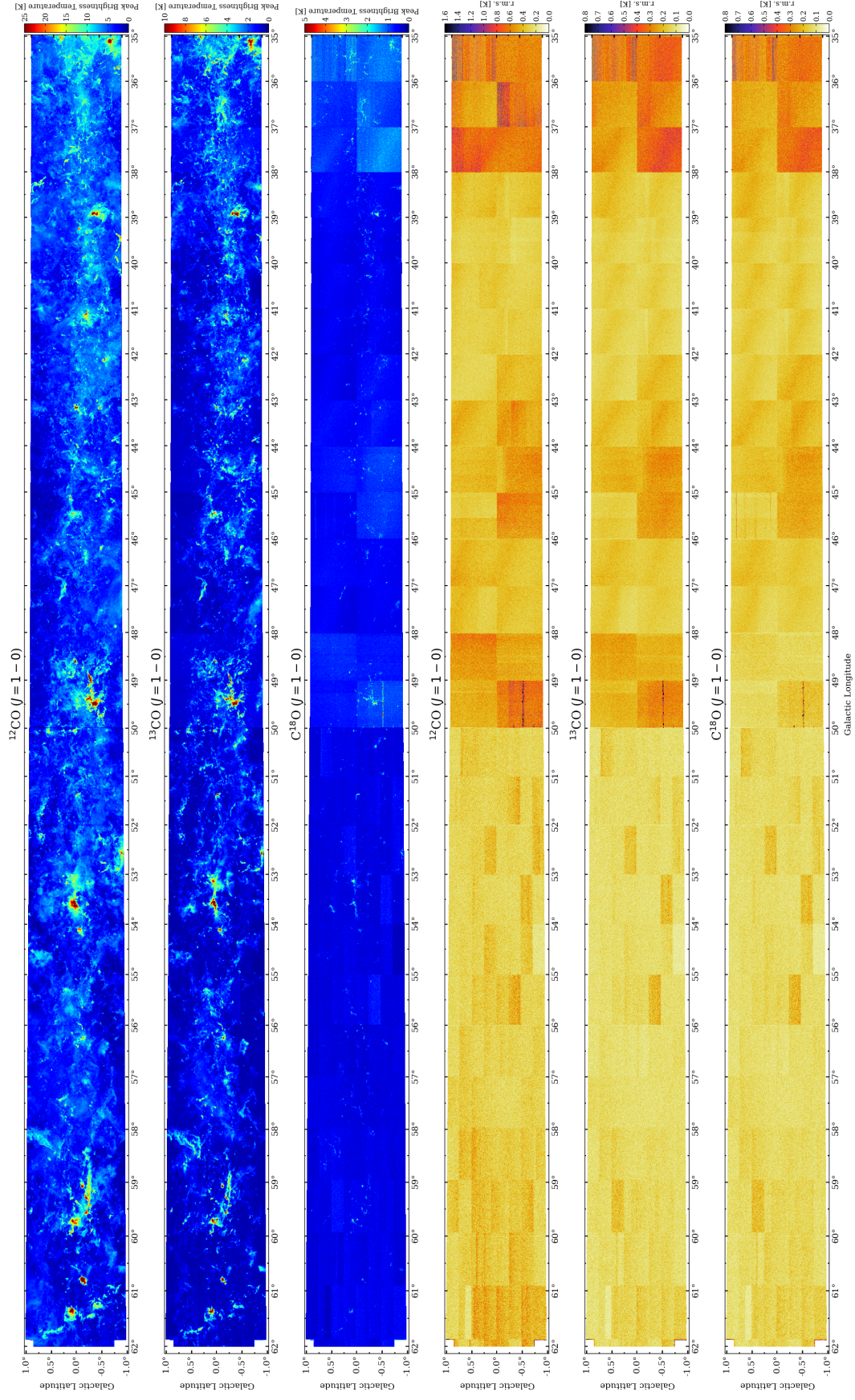


Fig. 1: (Continued)

3 Near-Far Labeling with a Convolutional Neural Network Model

3.1 Model architecture

We propose a Near-Far decision model based on a CNN, which is generally strong in image recognition. The model’s input data consist of two types: sensory data \mathbf{X}_i and a two-dimensional (2D) vector \mathbf{z}_i . The sensory data \mathbf{X}_i indicate a ^{12}CO ($J = 1 - 0$) cube (101 spatial pixels \times 101 spatial pixels \times 7 velocity channels). The 2D vector \mathbf{z}_i consists of two values, z_{near} and z_{far} , which indicate the floats from the Galactic disk ($D \sin b$, where D [kpc] and b [$^\circ$] are the distance and the Galactic latitude, respectively) when the inputted cloud is “Near” and “Far,” respectively. Using \mathbf{z}_i as an input, we were able to suppress the presence of clouds that were too far from the Galactic disk, thus slightly enhancing the accuracy of the model for the training dataset. The proposed CNN model can be formulated as follows.

$$y_i = f(\mathbf{X}_i, \mathbf{z}_i; \Theta), \quad (1)$$

where Θ denotes the set of parameters to be trained. Figure 2 shows in detail the architecture of the CNN model f . The CNN model f consists of three convolution layers, followed by two fully connected layers. We inserted an average pooling layer after the first convolution layer to reduce the input size and make the model more robust. We added “dropout” to suppress overfitting. The ReLU function and the Sigmoid function were used as activation functions for the middle and final fully connected layers, respectively. The output is a single value, $y_i \in [0, 1]$, which indicates whether the input is “Near” or “Far.” This model was implemented using the Python package Tensorflow, and the total number of parameters Θ was 522,435. We minimized this loss when training the CNN.

$$L(y_i, \hat{y}_i) = -\hat{y}_i \log y_i, \quad (2)$$

where $\hat{y}_i \in \{0, 1\}$ represents the binary-annotated values of the training data. The parameter set Θ was optimized through training.

3.2 Molecular clouds for the dataset with Near–Far annotations

The molecular clouds listed in the WISE HII region catalog³ (Anderson et al. 2014) as the dataset. Among the HII regions located in region ($l = 61^\circ.8 - 10^\circ.2$, $|b| < 0^\circ.8$), we selected only those that satisfied the following conditions: 1) HII regions with a label of “Near” or “Far,” 2) HII regions with associated ^{12}CO ($J = 1 - 0$) emissions; 3) HII regions with a ratio of far distance to near distance greater than two, i.e., regions other than those near the tangent. In addition, several local clouds with line-of-sight velocities of $0 - 10 \text{ km s}^{-1}$ were added as “Near” clouds. The number of “Near” and

³ <http://astro.phys.wvu.edu/wise/>

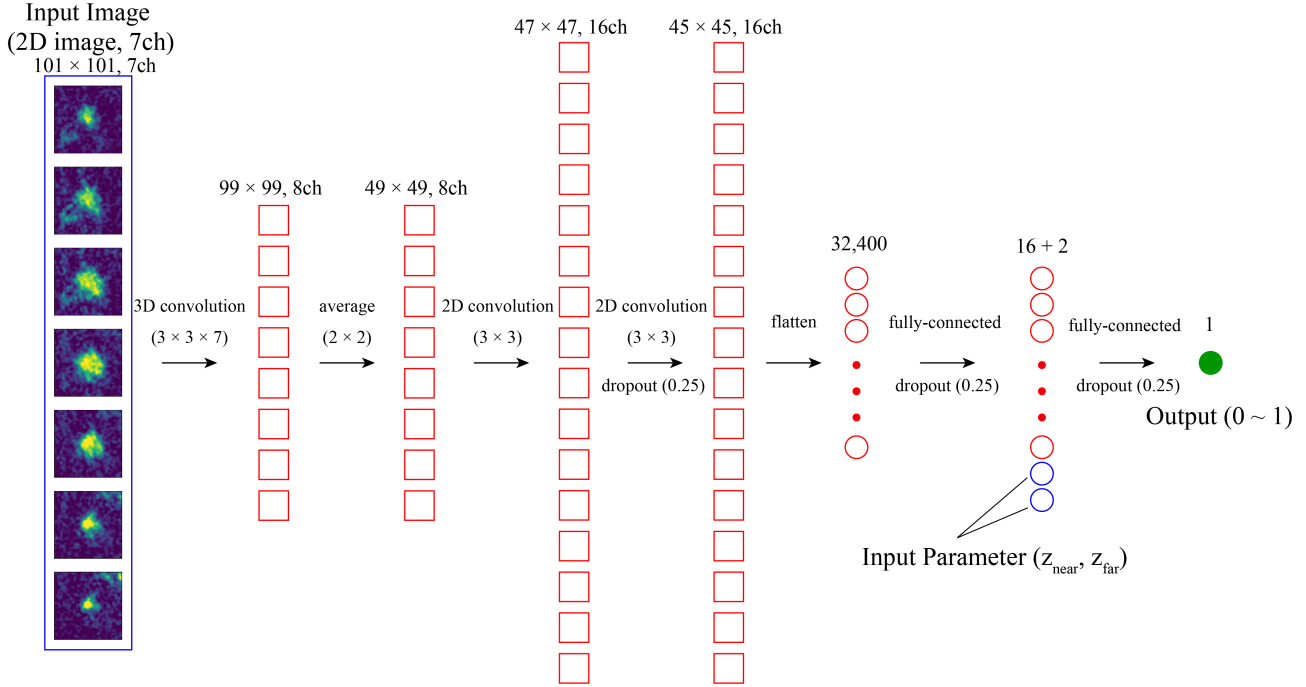


Fig. 2: CNN’s architecture. Blue, red, and green indicate input data, feature values, and output, respectively.

“Far” molecular clouds was 91 and 159, respectively.

3.3 Training of model

We randomly divided the dataset into five groups (four training datasets and one validation dataset), after which we trained and evaluated the model using cross-validation (Figure 3). After dividing the original dataset, the training sets were augmented (random rotation, random flipping, and addition of a random small offset) up to a total of 10,000 samples.

At every epoch, the sum of the loss values over the samples in the validation set (validation loss) was monitored. If no improvement was made for more than 50 epochs, the training was terminated, and the model parameters at the checkpoint (dot markers in Figure 3) with the minimum validation loss were saved. The average percentage of correct answers in the validation data throughout the training was approximately 76%.

3.4 Distance determination for each voxel

We applied the five models to all voxels that required inference, that is, $v_{\text{LSR}} > 0 \text{ km s}^{-1}$ (inside the orbit of the solar system for the 1st quadrant). To reduce the computational cost, the inference was performed every seven pixels in the spatial direction (the computational cost was reduced to $\sim 1/50$).

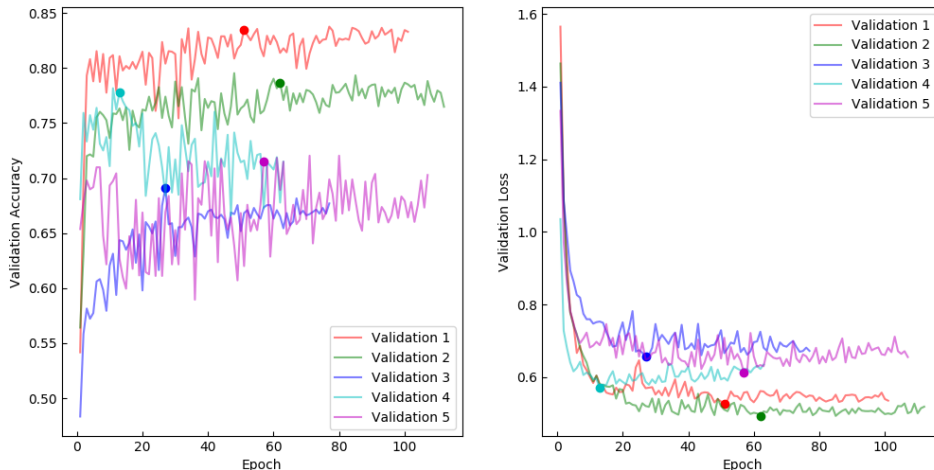


Fig. 3: Variation of the models’ “Accuracy” and “Loss” (cross-validation). The five dots indicate the saved point when the validation loss is the minimum.

Seven pix is sufficiently small for the input data shape (101×101), and by comparing the 7-pix sampled result with the full sampled result shown in Figure 4(b), we confirmed that it does not affect the inference accuracy. We used the averaged inference value of the five models.

Figure 4(a) shows the brightness temperature of the ^{12}CO ($J = 1 - 0$) emission ($v_{\text{LSR}} = 9.5 \text{ km s}^{-1}$) toward W49. There are ^{12}CO emissions from both the W49 molecular clouds and a nearby molecular cloud in this velocity channel. Figure 4(b) shows the predicted value of Near–Far using the CNN model. 0 and 1 refer to “Near” and “Far,” respectively. In this study, by binarizing the output value of the trained model using a threshold of 0.5, we can obtain the result of the Near–Far decision for the input. Specifically, if the output value is lower than the threshold of 0.5, the final decision is “Near”; otherwise, the final decision is “Far.” The area considered to be “Near” is the area inside the dotted line cyan contour in Figure 4(a). For these figures, it was confirmed that the Near–Far separation was accurate at least in this region, although the edge of the local molecular cloud is determined to be “Far.” As shown in Section 4.2, this effect is largely eliminated by taking a majority vote on the voxels that compose the cloud for each.

4 Cloud Identification and Distance Determination

4.1 Cloud identification

Cloud identification was performed using CLUMPFIND in PyCupid (Williams et al. 1994; Berry et al. 2007) for ^{12}CO , ^{13}CO , and C^{18}O ($J = 1 - 0$) cubes. The identification parameter “MINPIX”

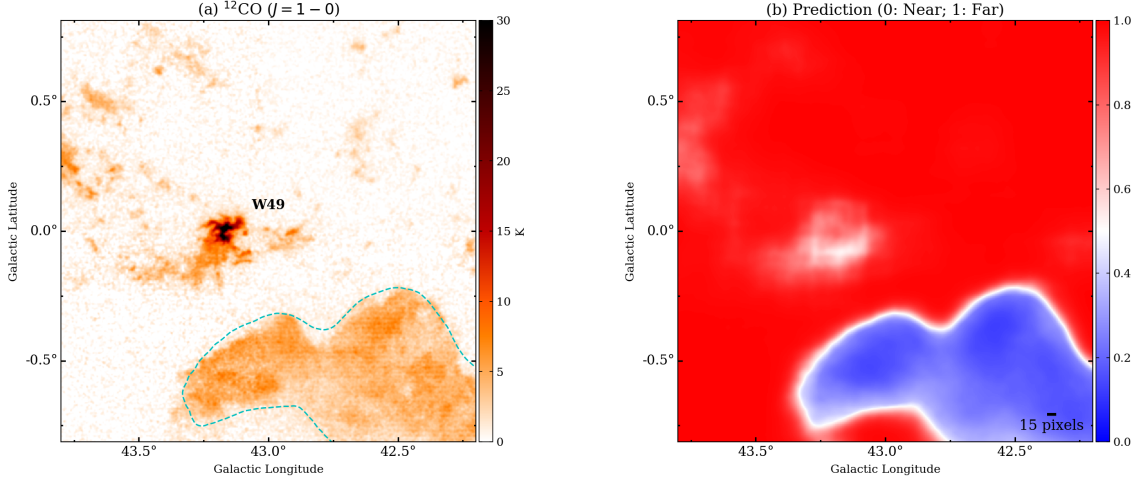


Fig. 4: (a) Brightness temperature of the ^{12}CO ($J = 1 - 0$) emission, ($v_{\text{LSR}} = 9.5 \text{ km s}^{-1}$) toward W49. The cyan dotted-line indicates where the predicted value is 0.5 in (b). (b) Predicted value of Near–Far by the CNN model. The values 0 and 1 refer to “Near” and “Far,” respectively.

(minimum number of voxels) was set to 500, 500, and 125 for ^{12}CO , ^{13}CO , and C^{18}O ($J = 1 - 0$), respectively, and “LEVEL” (contour levels) were set to [1.5 K (typically $\sim 1\sigma$), 5.0 K ($\sim 3\sigma$), 10.0 K, 15.0 K, ...], [1.0 K (typically $\sim 1\sigma$), 2.5 K ($\sim 3\sigma$), 5.0 K, 7.5 K, ...], and [1.0 K (typically $\sim 1\sigma$), 2.0 K (typically $\sim 2\sigma$), 3.0 K, 4.0 K, ...] for ^{12}CO , ^{13}CO , and C^{18}O ($J = 1 - 0$), respectively. The typical T_{rms} values of the three lines in the noisy regions are approximately 1.5 K, 1.0 K, and 1.0 K for ^{12}CO , ^{13}CO , and C^{18}O ($J = 1 - 0$), respectively. Therefore, we set “MINPIX” to be higher than in typical use cases to prevent the detection of the noise as the cloud. Note that the choice of these parameters may affect the results (the mass function in particular). Pineda et al. (2009) proposed that the CLUMPFIND parameter “stepsize” has a significant impact on the mass function when applied to three-dimensional (3D) data. In this study, a uniform, albeit arbitrary, parameter was applied although the noise levels and distances varied from region to region.

For the C^{18}O data, the four regions ($l(\text{degree}), b(\text{degree}) = (49.98\text{--}49.96, -0.38\text{--} -0.35)$, $(50.00\text{--}49.00, -0.58\text{--} -0.54)$, $(32.02\text{--}32.00, 0.00\text{--} +1.00)$, $(33.01\text{--}33.00, 0.00\text{--} +1.00)$) were removed because the noise level was too high ($> 5 \text{ K}$ typically). As a result, 142933, 37963, and 6664 clouds were identified in the ^{12}CO , ^{13}CO , and C^{18}O ($J = 1 - 0$) data cubes, respectively (hereafter referred to as ^{12}CO clouds, ^{13}CO clouds, and C^{18}O clouds). The identified clouds are listed in Tables 1, 2, and 3.

4.2 Distance determination for each identified cloud

Distance information is required to determine the mass of the identified cloud. For each identified cloud, we listed the CNN inference values (Section 3.4) of the voxels contained in the cloud and counted the number of values greater than 0.5. If the counted number was a majority of the total number of voxels, we consider the cloud as “Far;” otherwise, it was considered “Near.” Kinematic distances were assigned to all identified clouds using this procedure. Figure 5 shows the l - v diagram of the ^{12}CO ($J = 1 - 0$) emission. The circles represent the position of the ^{12}CO clouds, whereas the blue and red represent the “Near” and “Far” cloud, respectively. Figure 6 shows the integrated intensity map of the ^{13}CO ($J = 1 - 0$) emission toward sample regions, (a) the $l = 43^\circ$ region and (b) the $l = 24^\circ$ region. The cyan and red clouds indicate the “Near” and “Far” clouds, respectively. The results of a more detailed analysis of these molecular clouds are discussed in Paper II.

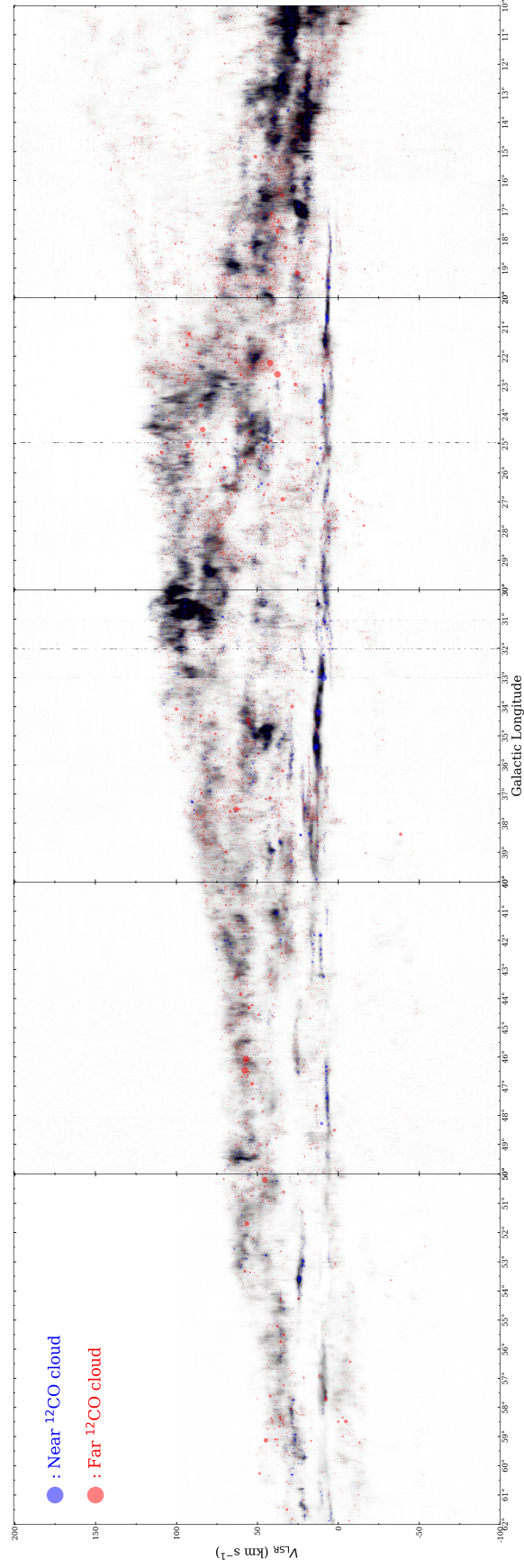


Fig. 5: l - v diagram of the ^{12}CO ($J = 1 - 0$) emission. The circles represent the position of the ^{12}CO clouds. The size of the circle is proportional to the area of the cloud. The blue and red circles refer to the “Near” and “Far” clouds, respectively.

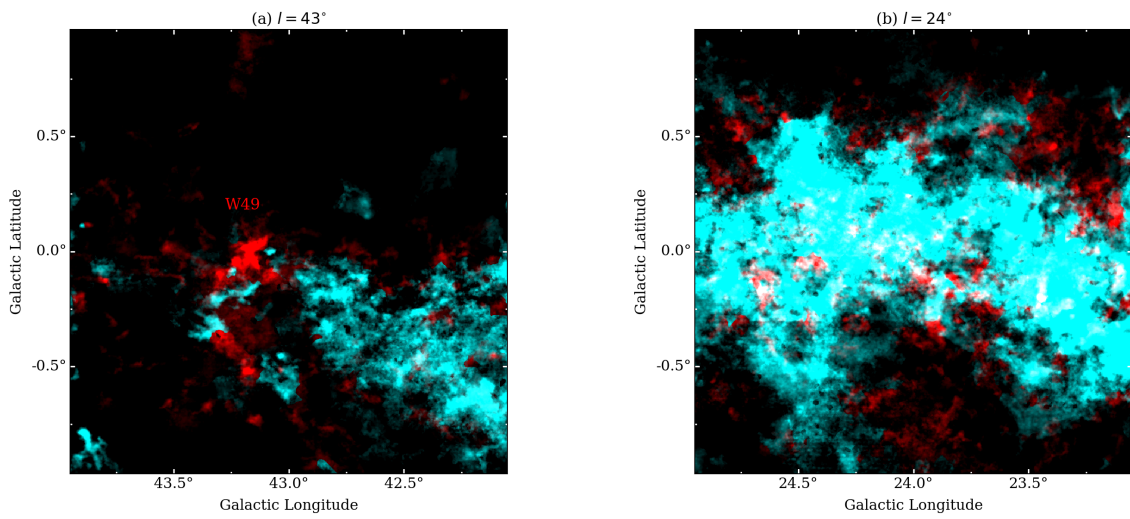


Fig. 6: Integrated intensity map of the ^{13}CO ($J = 1 - 0$) emission toward the (a) $l = 43^\circ$ region and (b) $l = 24^\circ$ region. The cyan and red clouds indicate the “Near” clouds and “Far” clouds, respectively.

Table 1: Molecular clouds identified in the ^{12}CO ($J = 1 - 0$) data

ID	l [$^\circ$]	b [$^\circ$]	v_{LSR} [km s^{-1}]	n_{vox}	σ_v [km s^{-1}]	$T_{12\text{CO}}$ [K]	$T_{13\text{CO}}$ [K]	$T_{\text{C}^{18}\text{O}}$ [K]	$w_{12\text{CO}}$ [K km s^{-1} degree 2]	$w_{13\text{CO}}$ [K km s^{-1} degree 2]	$w_{\text{C}^{18}\text{O}}$ [K km s^{-1} degree 2]	NF	D [kpc]	M_{LTE} [M_\odot]	R_{gal} [kpc]	s [pc]
12CO-000001	10.621	-0.381	-4.12	45358	3.00	47.6	24.0	5.0	1.69e+00	4.21e-01	7.42e-02	F(1.00)	16.89	1.53e+06	9.00	10.31
12CO-000002	10.628	-0.336	-3.48	31397	2.97	42.3	21.7	8.0	1.14e+00	2.72e-01	4.86e-02	F(1.00)	16.74	8.94e+05	8.86	8.27
12CO-000003	10.595	-0.367	-2.17	28521	2.86	41.7	15.2	4.5	1.02e+00	2.39e-01	3.54e-02	F(1.00)	16.46	7.33e+05	8.58	8.94
...																
12CO-141540	61.712	0.752	5.04	2633	0.54	5.0	0.6	-0.1	2.14e-02	1.23e-03	2.78e-04	N(0.37)	0.43	8.60e-01	7.96	0.33
12CO-141541	61.216	0.303	34.31	11376	1.35	5.0	0.4	-0.2	9.28e-02	1.35e-02	2.34e-04	F(0.97)	3.92	8.29e+02	6.99	3.93
12CO-141542	60.168	-0.244	25.86	1212	1.16	5.0	0.4	0.3	1.12e-02	8.84e-04	6.23e-05	F(0.95)	5.60	1.09e+02	7.24	1.02

l , b , and v_{LSR} are the peak positions of the ^{12}CO ($J = 1 - 0$) emission. n_{vox} is the number of voxels that the cloud contains. σ_v is the intensity-weighted standard deviation of the velocity. $T_{12\text{CO}}$, $T_{13\text{CO}}$, and $T_{\text{C}^{18}\text{O}}$ are the respective intensities of the ^{12}CO ($J = 1 - 0$), ^{13}CO ($J = 1 - 0$), and C^{18}O ($J = 1 - 0$) emission at the peak position. $w_{12\text{CO}}$, $w_{13\text{CO}}$, and $w_{\text{C}^{18}\text{O}}$ are the combined intensities of the three emissions, respectively. NF refers to Near (N) or Far (F) assigned by us. Decimals in parentheses indicate the confidence of the inference (median value of the inference by five models in all voxels); closer to 0.0 means “Near”, and closer to 1.0 means “Far”. D is the kinematic distance to the cloud. M_{LTE} is the mass of the cloud derived from LTE analysis using the peak brightness temperature of the ^{12}CO ($J = 1 - 0$) and the brightness temperature of the ^{13}CO ($J = 1 - 0$). We adopted an abundance ratio [$^{13}\text{CO}/\text{H}_2$] of 1.5×10^{-6} . R_{gal} is the Galactocentric distance to the cloud. s is the size of the cloud ($D \tan(\sqrt{\sigma_l \sigma_b})$), where σ_l and σ_b are the intensity-weighted standard deviation values along the Galactic Longitude axis and Galactic Latitude axis, respectively). (This table is available in its entirety in machine-readable form.)

Table 2: Molecular clouds identified in the ^{13}CO ($J = 1 - 0$) data.

ID	l [$^\circ$]	b [$^\circ$]	v_{LSR} [km s^{-1}]	n_{vox}	σ_v [km s^{-1}]	$T_{12\text{CO}}$ [K]	$T_{13\text{CO}}$ [K]	$T_{\text{C}^{18}\text{O}}$ [K]	$w_{12\text{CO}}$ [K km s^{-1}]	$w_{13\text{CO}}$ [K km s^{-1}]	$w_{\text{C}^{18}\text{O}}$ [K km s^{-1}]	NF	D [kpc]	M_{LTE} [M_\odot]	R_{gal} [kpc]	s [pc]	
												degree 2					degree 2
13CO-000001	10.621	-0.379	-2.83	12370	2.09	46.2	26.6	7.9	8.41e-01	2.35e-01	4.07e-02	F(1.00)	16.60	8.44e+05	8.72	6.36	
13CO-000002	10.628	-0.336	-4.12	7263	1.73	41.9	22.9	8.1	5.18e-01	1.57e-01	3.26e-02	F(1.00)	16.89	5.40e+05	9.00	4.79	
13CO-000003	10.595	-0.365	-2.83	16032	1.85	40.2	18.0	4.3	8.39e-01	2.25e-01	3.32e-02	F(1.00)	16.60	7.09e+05	8.72	8.34	
...																	
13CO-037607	60.335	-0.769	28.46	835	0.49	6.8	2.6	0.4	1.84e-02	4.59e-03	1.61e-04	N(0.35)	3.00	1.87e+02	7.16	0.62	
13CO-037608	61.726	0.575	20.65	683	0.55	9.2	2.5	0.3	1.68e-02	3.80e-03	1.99e-04	N(0.25)	2.01	7.32e+01	7.41	0.50	
13CO-037609	61.452	-0.492	28.46	1625	0.89	5.2	2.5	0.2	2.58e-02	7.67e-03	3.47e-04	F(0.95)	4.21	5.92e+02	7.17	1.30	

l , b , and v_{LSR} are the peak positions of the ^{13}CO ($J = 1 - 0$) emission. n_{vox} is the number of voxels that the cloud contains. σ_v is the intensity-weighted standard deviation of the velocity. $T_{12\text{CO}}$, $T_{13\text{CO}}$, and $T_{\text{C}^{18}\text{O}}$ are the intensities of the ^{12}CO ($J = 1 - 0$), ^{13}CO ($J = 1 - 0$), and C^{18}O ($J = 1 - 0$) emission, respectively, at the peak position. $w_{12\text{CO}}$, $w_{13\text{CO}}$, and $w_{\text{C}^{18}\text{O}}$ are respectively the combined intensities of the three emissions. NF indicates Near (N) or Far (F), which we assigned. Decimals in parentheses indicate the confidence of the inference (median value of the inference by five models in all of the voxels); closer to 0.0 means ‘Near’, and closer to 1.0 means ‘Far’. D is the kinematic distance to the cloud. M_{LTE} is the mass of the cloud derived from LTE analysis using the peak brightness temperature of ^{12}CO ($J = 1 - 0$) and the brightness temperature of ^{13}CO ($J = 1 - 0$). We adopted an abundance ratio $[^{13}\text{CO}]/[\text{H}_2]$ of 1.5×10^{-6} . R_{gal} is the Galactocentric distance to the cloud. s is the size of the cloud ($D \tan(\sqrt{\sigma_l \sigma_b})$), where σ_l and σ_b are the intensity-weighted standard deviation values along the Galactic longitude axis and Galactic latitude axis, respectively.) (This table is available in its entirety in machine-readable form.)

Table 3: Molecular clouds identified in the C¹⁸O ($J = 1 - 0$) data.

ID	l [°]	b [°]	v_{LSR} [km s ⁻¹]	n_{vox}	σ_v [km s ⁻¹]	$T_{12\text{CO}}$ [K]	$T_{13\text{CO}}$ [K]	$T_{\text{C}^{18}\text{O}}$ [K]	$w_{12\text{CO}}$ [K km s ⁻¹]	$w_{13\text{CO}}$ [K km s ⁻¹]	$w_{\text{C}^{18}\text{O}}$ [K km s ⁻¹]	NF	D [kpc]	M_{LTE} [M _⊙]	R_{gal} [kpc]	s [pc]
												degree ²	degree ²			
C180-000001	10.633	-0.336	-3.48	1414	1.18	41.2	22.0	9.1	1.42e-01	5.26e-02	1.39e-02	F(1.00)	16.74	383431.88	8.86	2.98
C180-000002	10.623	-0.381	-2.83	2630	1.51	45.3	26.5	8.4	2.85e-01	1.02e-01	2.31e-02	F(1.00)	16.60	682457.99	8.72	3.45
C180-000003	10.210	-0.320	12.12	15549	2.07	13.1	11.0	7.4	7.45e-01	3.89e-01	1.21e-01	N(0.12)	1.87	34758.15	6.32	0.88
...																
C180-006592	61.362	0.086	21.30	902	0.83	45.6	20.8	3.0	1.05e-01	3.87e-02	4.48e-03	N(0.17)	2.05	2026.41	7.39	0.54
C180-006593	60.779	-0.122	20.65	681	1.13	36.7	13.8	2.2	9.92e-02	2.99e-02	3.15e-03	N(0.15)	1.91	1330.55	7.41	0.30
C180-006594	61.674	0.287	20.65	187	0.41	10.9	7.1	2.1	7.03e-03	3.79e-03	8.64e-04	N(0.23)	2.00	155.32	7.41	0.40

l , b , and v_{LSR} are the peak positions of the C¹⁸O ($J = 1 - 0$) emission. n_{vox} indicates the number of voxels that the cloud contains. σ_v is the intensity-weighted standard deviation of the velocity. $T_{12\text{CO}}$, $T_{13\text{CO}}$, and $T_{\text{C}^{18}\text{O}}$ are the intensities of the ¹²CO ($J = 1 - 0$), ¹³CO ($J = 1 - 0$), and C¹⁸O ($J = 1 - 0$) emission, respectively, at the peak position. $w_{12\text{CO}}$, $w_{13\text{CO}}$, and $w_{\text{C}^{18}\text{O}}$ are the combined intensities of the three emissions, respectively. NF indicates Near (N) or Far (F), which we assigned. Decimals in parentheses indicate the confidence of the inference (median value of the inference by five models in the all voxels); closer to 0.0 means “Near”, and closer to 1.0 means “Far”. D is the kinematic distance to the cloud. M_{LTE} is the mass of the cloud derived from LTE analysis using the peak brightness temperature of the ¹²CO ($J = 1 - 0$) and the brightness temperature of the C¹⁸O ($J = 1 - 0$). We adopted an abundance ratio $[\text{C}^{18}\text{O}]/[\text{H}_2]$ of 1.7×10^{-7} . R_{gal} is the Galactocentric distance to the cloud. s is the size of the cloud ($D \tan(\sqrt{\sigma_l \sigma_b})$), where σ_l and σ_b are the intensity-weighted standard deviation values along the Galactic longitude axis and Galactic latitude axis, respectively). (This table is available in its entirety in machine-readable form.)

4.3 Mass, size, and velocity dispersion of the clouds

By assuming local thermodynamic equilibrium (LTE), we determined the column densities of ^{13}CO for ^{12}CO clouds and ^{13}CO clouds. In addition, we derived the column densities of C^{18}O for the C^{18}O clouds. The equations for the LTE analysis are the same as those used in Kawamura et al. (1998), Shimajiri et al. (2014) and Nishimura et al. (2015).

$$T_{\text{ex}} = \frac{T_0}{\ln[1 + (T_0/(T_{\text{peak}}(^{12}\text{CO}) + 0.84))]} \text{ [K]} \quad (3)$$

$$J(T) \equiv \frac{1}{\exp(T_0/T) - 1} \quad (4)$$

$$\tau_{^{13}\text{CO}} = -\ln \left\{ 1 - \frac{T_{\text{MB}}(^{13}\text{CO})}{T_0[J(T_{\text{ex}}) - 0.164]} \right\} \quad (5)$$

$$N_{^{13}\text{CO}} = 2.42 \times 10^{14} \left\{ \frac{\tau_{^{13}\text{CO}} \Delta V T_{\text{ex}}}{1 - \exp[-T_0/T_{\text{ex}}]} \right\} \text{ [cm}^{-2}\text{]} \quad (6)$$

$$\tau_{\text{C}^{18}\text{O}} = -\ln \left\{ 1 - \frac{T_{\text{MB}}(\text{C}^{18}\text{O})}{T_0[J(T_{\text{ex}}) - 0.1666]} \right\} \quad (7)$$

$$N_{\text{C}^{18}\text{O}} = 2.42 \times 10^{14} \left\{ \frac{\tau_{\text{C}^{18}\text{O}} \Delta V T_{\text{ex}}}{1 - \exp[-T_0/T_{\text{ex}}]} \right\} \text{ [cm}^{-2}\text{]} \quad (8)$$

Here, T_{ex} and $T_{\text{peak}}(^{12}\text{CO})$ are the excitation and peak brightness temperatures of the ^{12}CO voxels in units of K (T_{MB} scale), respectively. The same value of T_{ex} was used for each cloud. $T_{\text{MB}}(^{13}\text{CO})$ and $T_{\text{MB}}(\text{C}^{18}\text{O})$ are the brightness temperatures in units of K. T_0 are 5.53 K for Equation (3), 5.29 K for Equations (5) and (6), and 5.27 K for Equations (7) and (8), respectively. ΔV is the velocity grid size of the cube, 0.65 km s^{-1} . The cloud mass was calculated from the total H_2 column density.

$$\left(\frac{M_{\text{cloud}}}{M_{\odot}} \right) = 4.05 \times 10^{-1} \mu_{\text{H}_2} \left(\frac{m_{\text{H}}}{\text{kg}} \right) \left(\frac{d}{\text{pc}} \right)^2 \left(\frac{\Delta l}{\text{arcmin}} \right) \left(\frac{\Delta b}{\text{arcmin}} \right) \left(\frac{N_{\text{H}_2}}{\text{cm}^{-2}} \right), \quad (9)$$

where $\mu_{\text{H}_2} \sim 2.7$ is the mean molecular weight per H_2 molecule, m_{H} is the mass of atomic hydrogen, d is the distance, and Δl and Δb are the spatial grid sizes.

Figure 7 shows the detection limit of the cloud mass in this study as a function of the distance to clouds. Three representative T_{ex} values of 10, 20, and 30 K were adopted. Figure 8 (a) shows the histograms of the mass of the ^{12}CO clouds (red), ^{13}CO clouds (green), and C^{18}O clouds (blue) with a distance of $< 8.15 \text{ kpc}$. We adopted abundance ratios $[^{13}\text{CO}]/[\text{H}_2]$ and $[\text{C}^{18}\text{O}]/[\text{H}_2]$ of 1.5×10^{-6} and 1.7×10^{-7} , respectively (Dickman 1978; Frerking et al. 1982). Figure 8 (b) is the same as Figure 8 (a), but the vertical axis is dN/dM . It appears that $dN/dM \propto M^{-\alpha}$ in the mass range of $M > 3 \times 10^3 M_{\odot}$, whose value is above the mass detection limit shown in Figure 7. For the least-squares fitting, α was found to be 2.30 ± 0.11 , 2.33 ± 0.15 , and 2.44 ± 0.17 for the ^{12}CO , ^{13}CO , and C^{18}O clouds, respectively. Figures 8 (c) and (d) are the same as in Figures 8 (a) and (b), but with cloud

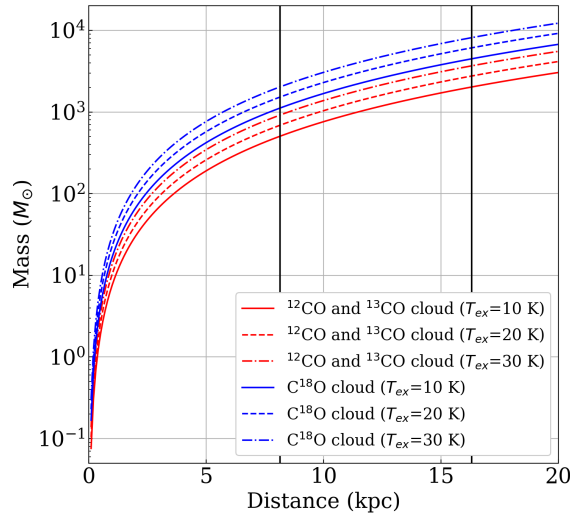


Fig. 7: Detection limit of the cloud mass in this study as a function of distance to clouds. The two thick vertical lines indicate 8.15 kpc and 16.3 kpc.

distances of < 16.3 kpc. The mass detection limits in 16.3 kpc were approximately $1 \times 10^4 M_{\odot}$, as shown in Figure 7. Within this mass range, the slopes are steeper than those in Figure 8 (b). For example, with respect to the cloud mass function, Rosolowsky et al. (2007) reported a similar α value of approximately 2.1 within an annulus of $2.1 \text{ kpc} < R_{\text{gal}} < 4.1 \text{ kpc}$ for M33. In addition, Pineda et al. (2009) found $\alpha = 2.4$ for the standard CLUMPFIND parameters in the Perseus Molecular Cloud Complex, which has a value that is similar to our results.

Figure 9 shows the scatter plot of the size and σ_v of the ^{13}CO clouds (gray points). The definitions of size and σ_v are the same as those used in Solomon et al. (1987) and Heyer et al. (2009), and they are the intensity-weighted standard deviation values. The blue and red points show the results of Heyer et al. (2009) (A1) using the area defined in Solomon et al. (1987) and A2, using the area defined by the GRS data). Heyer et al. (2009) analyzed the GRS data and re-examined the properties of the Galactic molecular clouds tabulated by Solomon et al. (1987). The “Near” or “Far” for most of the clouds in Solomon et al. (1987) were determined using a well-matched size-line width relation. The black, blue, and red solid lines in Figure 9 indicate the linear least-squares fit for the gray, blue, and red points in a log-log space, respectively. The slopes were ~ 0.11 , ~ 0.36 , and ~ 0.22 for the gray, blue, and red points, respectively. The black dashed line in Figure 9 indicates $\sigma_v = s^{0.5}$, where s is the radius of the cloud in units of PC, indicating the slope of Larson’s law (Larson 1981). There is a size difference between Nobeyama 45-m data (this study) and Heyer et al. (2009). This is because of the angular resolution; the difference is small for A2 but significant for A1. However, σ_v increases

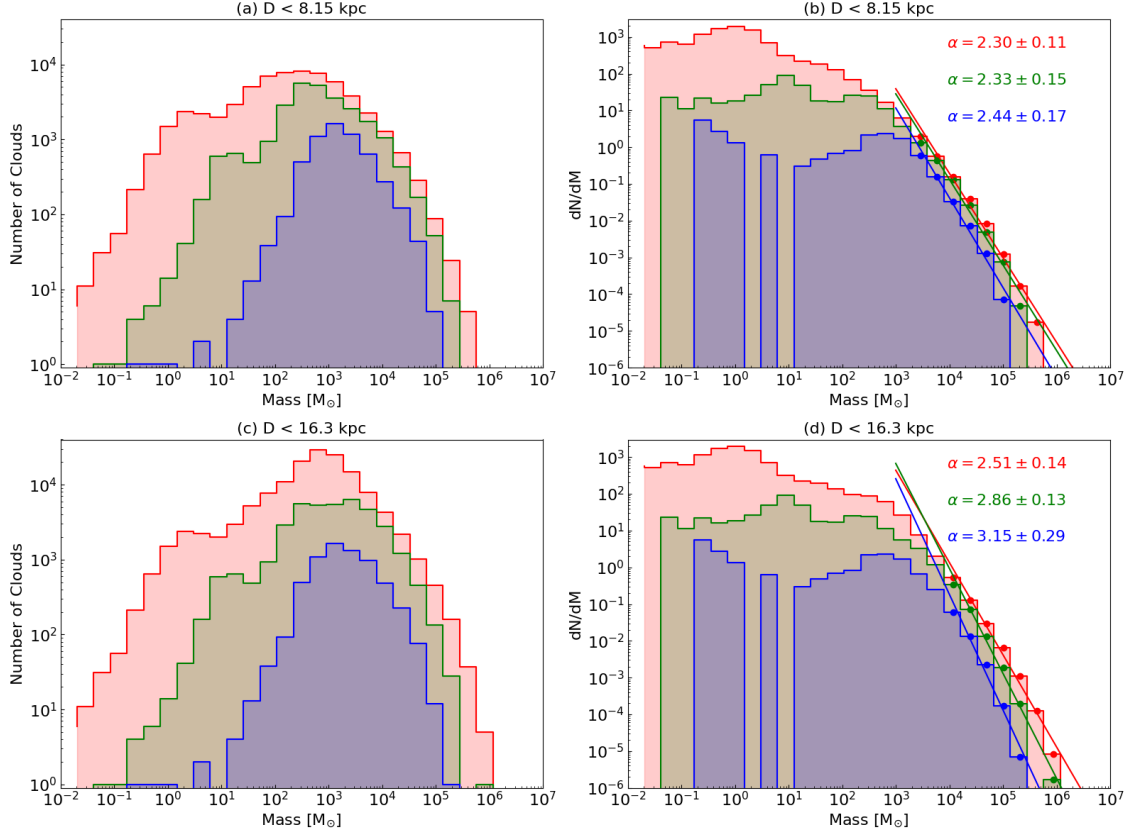


Fig. 8: (a) Histograms of the mass of the ^{12}CO clouds (red), ^{13}CO clouds (green), and C^{18}O clouds (blue) with a distance of < 8.15 kpc. (b) Same as the left, but the vertical axis is dN/dM . (c) and (d) are the same as (a) and (b), respectively, but with a distance of < 16.3 kpc.

according to the size, whereas the slope differs among the three. The slopes tended to become more gradual at higher angular resolutions; However, there may be a tendency for the slope to become steeper as the distance increases. In the future, we will analyze our results and discuss them in detail.

5 Face-on-view of the Galaxy

The distances between the clouds identified above were calculated. Then, we plotted the face-on-view maps of the column density of ^{13}CO for the ^{12}CO clouds and the column density of C^{18}O for the C^{18}O clouds, which were derived in Section 4.3. Figure 10 shows the face-on-view map of the ^{13}CO column density of the ^{12}CO clouds and the C^{18}O column density of the C^{18}O clouds. The solar system is the origin, and the cross mark represents the Galactic center. The tangential points and solar circles are shown by the small and large dotted circles, respectively. The angular and radial grid sizes of the map are $30''$ and 0.1 kpc, respectively. In the ^{13}CO column density map, several spiral arm-like structures and a hole can be observed at $(\theta, D) = (20^\circ, 7.5 \text{ kpc})$. This hole is also observed in the map

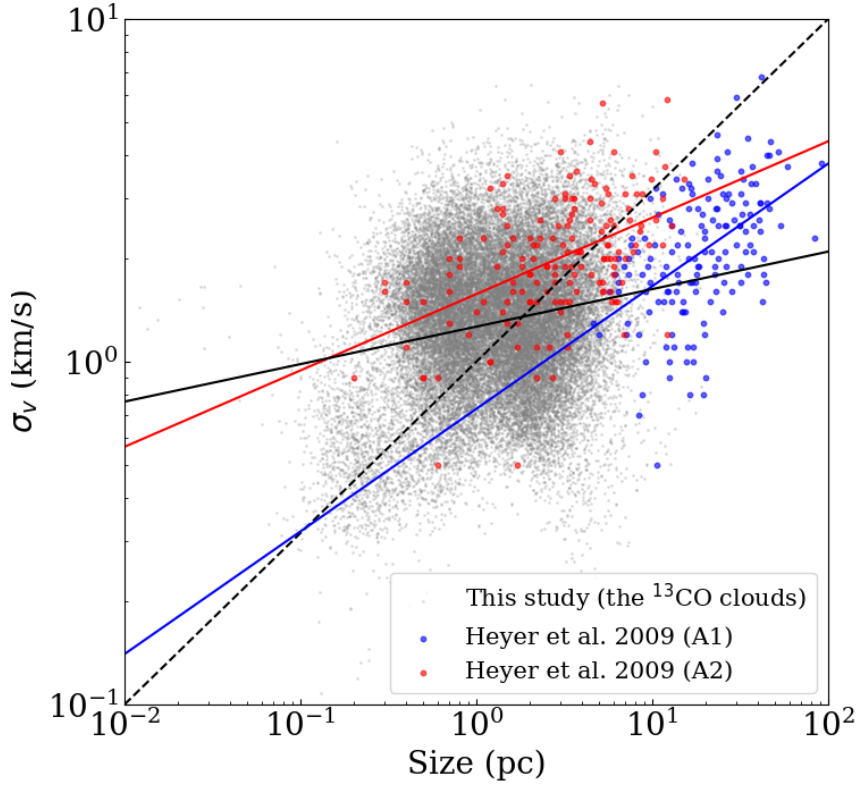


Fig. 9: Relation between the size and σ_v of the ^{13}CO clouds (gray points). The blue and red points show the results of Heyer et al. (2009). The black, blue, and red solid lines indicate the linear least-squares fit for the gray points, the blue points, and red points in a log-log space, respectively. The dashed-line indicates $\sigma_v = s^{0.5}$, where s is the size of the cloud in units of pc.

of Nakanishi & Sofue (2006). In contrast, in the C^{18}O , from the column density map, the C^{18}O cloud is mainly identified as a ring with a radius of ~ 4.5 kpc centered on the Galactic center.

Figure 11 shows a face-on-view map of the ^{13}CO column density of the ^{12}CO clouds, and the circles indicate the high-mass star-forming regions with the measured trigonometric parallaxes (Reid et al. 2019). The “long” bar (Wegg et al. 2015) is shown with a green dotted-line ellipse. The distribution of molecular gas corresponds well to the majority of high-mass star-forming regions. Molecular gas is also concentrated in the region of the bar end, which is where the W43 complex is located (Kohno et al. 2021).

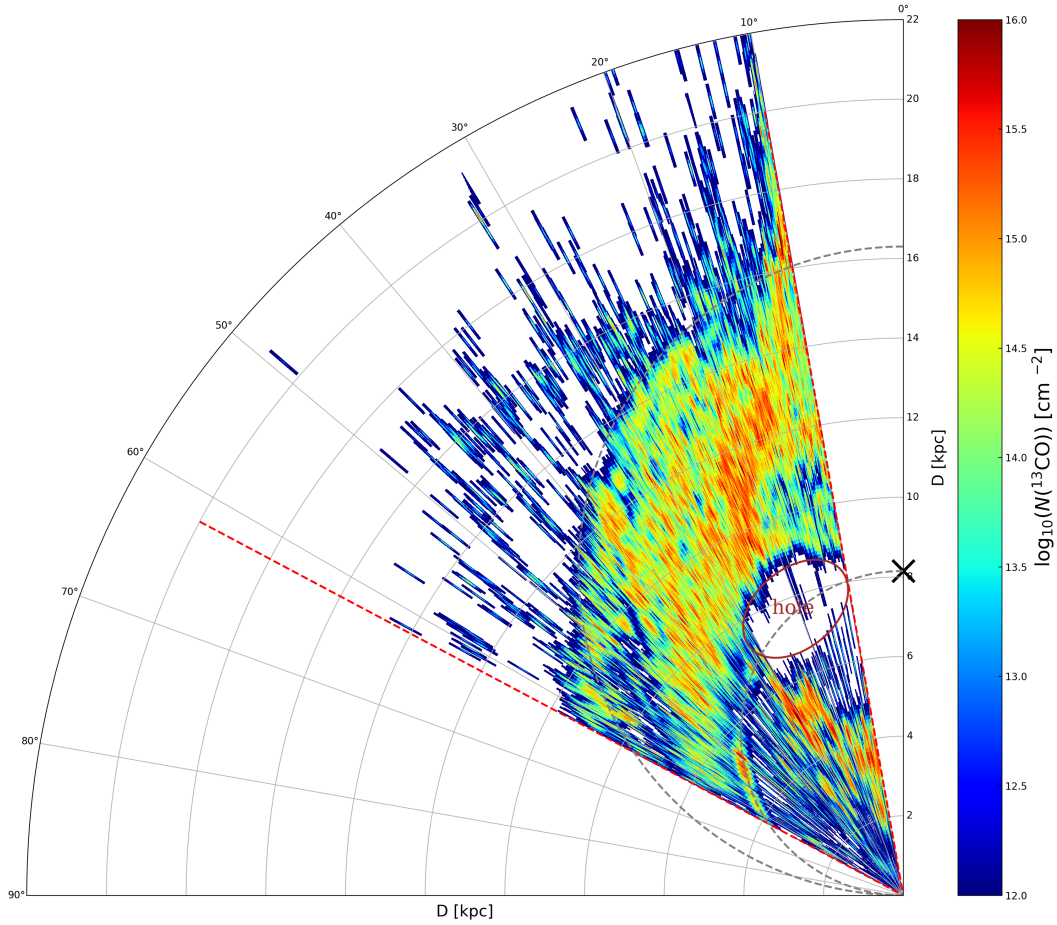


Fig. 10: Face-on-view map of the ^{13}CO column density of the ^{12}CO clouds and the C^{18}O column density of the C^{18}O clouds seen from the Galactic North pole. The solar system is the origin, while the cross mark indicates the Galactic center. The tangential points and the solar circle are shown by the small and large dotted-line circles, respectively. The Galaxy rotates in a clock-wise direction. The red ellipse shows the hole structure, which is also seen in Nakanishi & Sofue (2006)

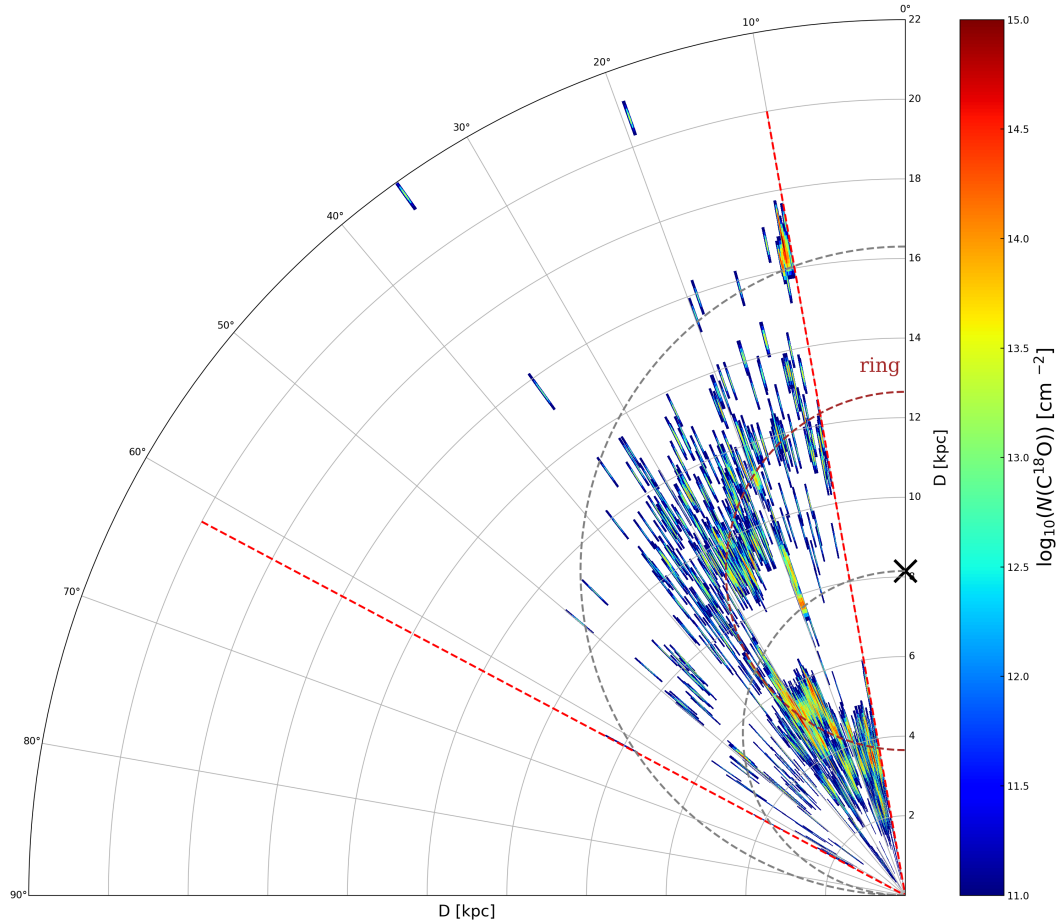


Fig. 10: (Continued)

6 Possible errors in our distance estimation

In our distance estimation, there are several possible errors that can be attributed to various assumptions and methods.

First, we assumed that all molecular clouds in the Galaxy follow the flat rotation. However, molecular clouds exhibit intrinsic motions that deviate from the rotation. The error that results from this is approximately 1 kpc, as discussed in a previous study (Nakanishi & Sofue 2006). Figures 12(a) and (b) show the calculated kinematic distance in the Galactic plane ($b = 0^\circ$). Typically, a deviation of $10 - 20 \text{ km s}^{-1}$ corresponds to approximately 1 kpc. For example, Stark (1984) reported that the one-dimensional (1D) r.m.s. velocity dispersion of molecular clouds in the Galaxy is 9 km s^{-1} .

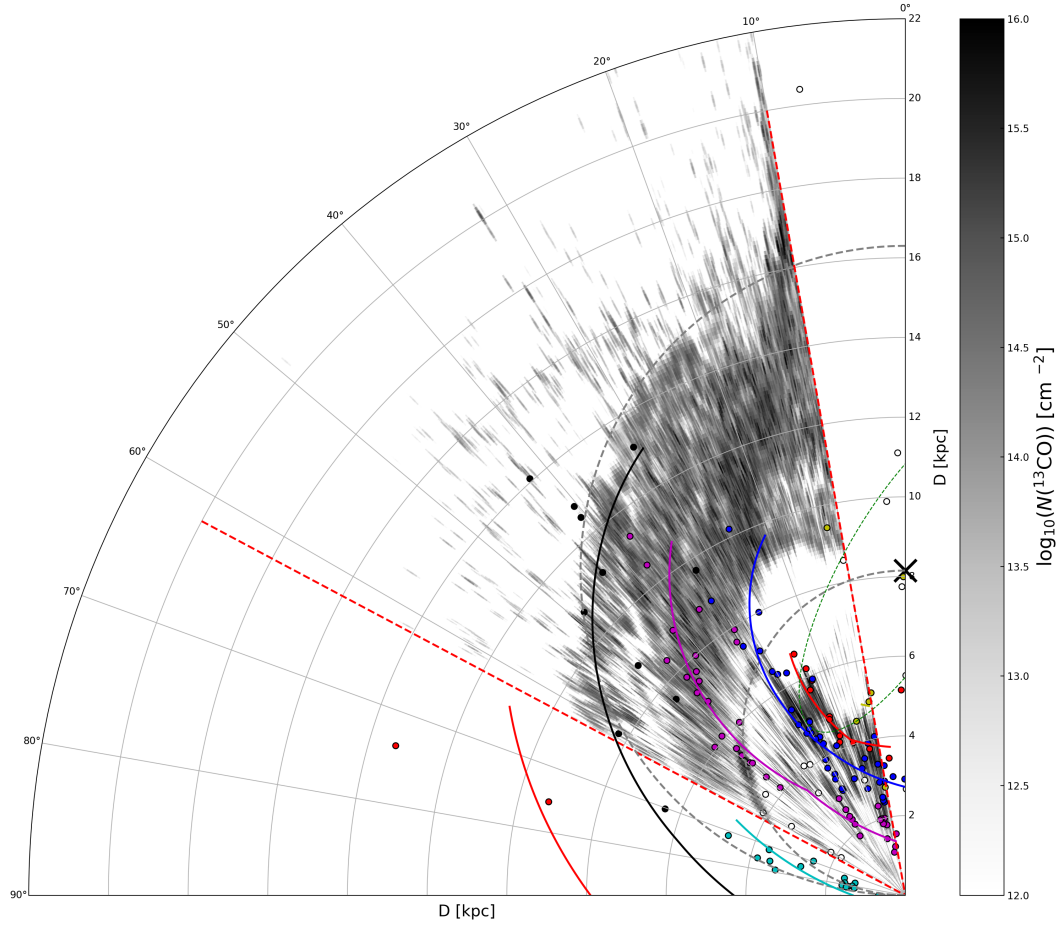


Fig. 11: Face-on-view map of the ^{13}CO column density of the ^{12}CO clouds seen from the Galactic North pole. The circle markers represent the high-mass star-forming regions with measured trigonometric parallaxes (Reid et al. 2019): 3 kpc arm, yellow; Norma–Outer arm, red; Scutum–Centaurus–OSC arm, blue; Sagittarius–Carina arm, purple; Local arm, cyan; Perseus’s arm, black; spurs or sources for which the arm assignment is unclear, white. The “long” bar (Wegg et al. 2015) is indicated with a green dotted-line ellipse.

Furthermore, there may be a specific velocity depending on the environment in the Galaxy (e.g., the bar end); thus, the hole structure shown in Figure 10 may be artificial. In fact, Zhang et al. (2014) reported that the peculiar motion of W43, which is located near the bar end, is approximately 20 km s^{-1} toward the Galactic Center by trigonometric parallax measurements of the masers. It is very likely that this peculiar motion was induced by the gravitational attraction of the bar.

Second, the error is due to bias in the teacher (molecular clouds for the dataset with Near–Far annotations) of the model. For the teacher dataset, we used only the molecular clouds associated with the HII regions. It is possible that they are essentially different from molecular clouds without HII regions, which may affect the results. However, it is difficult to measure the distances of molecular clouds without HII regions, and we cannot include them in the teacher dataset.

Third, we assumed that CO emission in a single voxel is derived from a single molecular cloud. It is possible that in some regions, “Near” clouds and “Far” clouds overlap in the Position–Position–Velocity (PPV) space. However, the angular resolution of the Nobeyama 45-m data that was used is high, and we therefore consider that there is a sufficiently low probability of the “Near” and “Far” cloud overlapping in the PPV space, although they cannot be estimated quantitatively. This may be revealed by future detailed numerical simulations of galaxies.

Fourth, errors in model inference may have affected the results. The accuracy of the model with respect to the teacher dataset was measured to be 76%; however, the degree of accuracy for the molecular clouds in the Galactic plane is not currently known. Figures 12(c) and (d) show the difference and ratio between the “Far” and “Near” solution. The closer to 0 ,km , s^{-1} , the greater is the loss when there were errors in “Near” -and “Far”. We plan to test the accuracy of the method in this study using pseudo-observational data obtained from numerical simulations of molecular gas in galaxies.

We checked our decision (“Near” or “Far”) for the clouds listed in Solomon et al. (1987) (SRBY). Clouds were selected from only within the region of the data. Table 4 lists the number of molecular clouds. The number of matches was 125 ($\sim 66\%$), which is the sum of the cases that both this study and SRBY identify as “Near” (98), as well as the case where both of them identify as “Far” (27). In particular, the number of clouds determined to be “Near” was higher in our inference than in SRBY. This result indicates that our inference may be more likely to produce “Near,” although the angular resolutions of our data and those of SRBY are generally different.

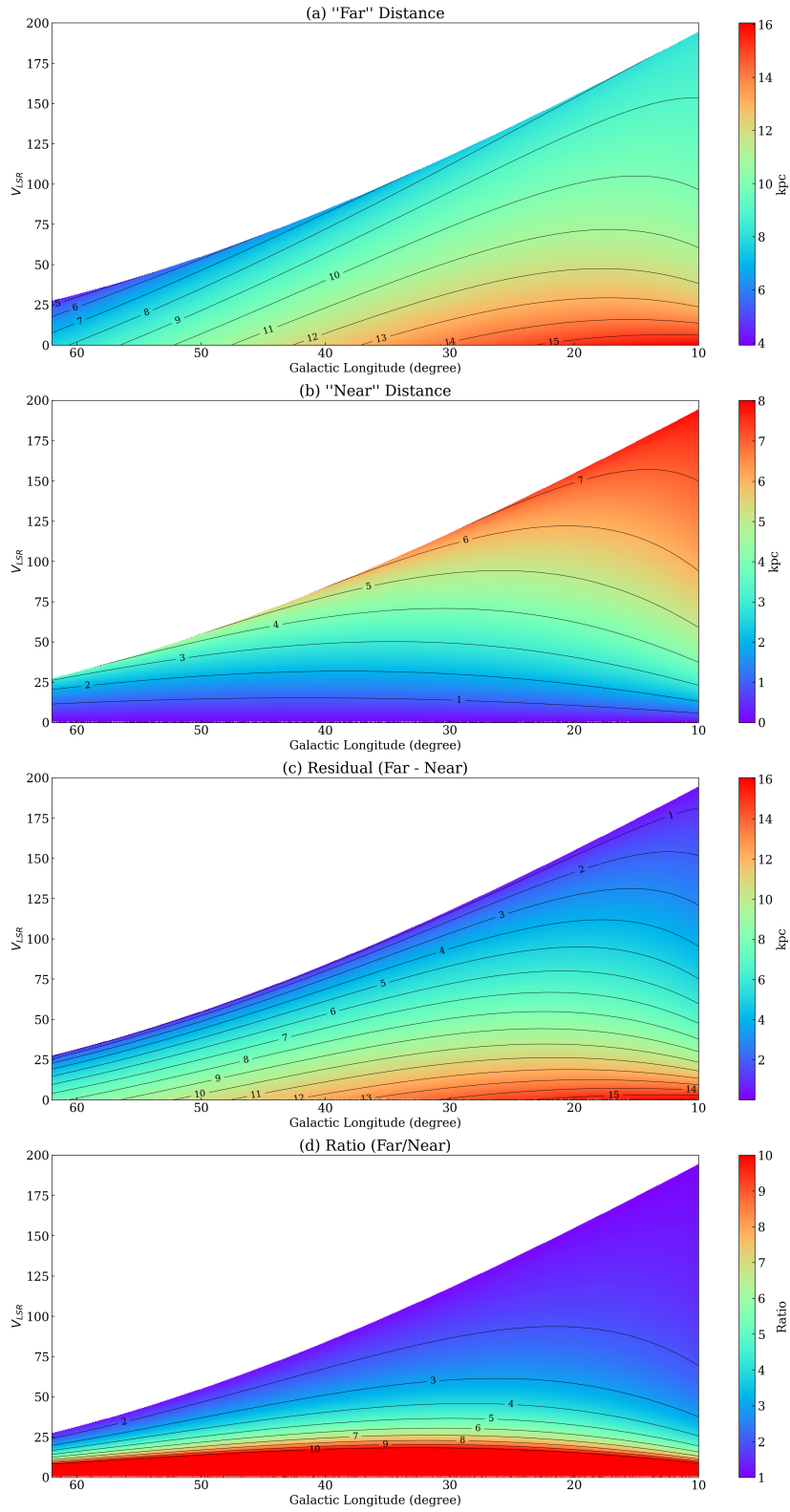


Fig. 12: Kinematic distance in the Galactic plane ($b = 0^\circ$) for the (a) "Far" solution and (b) "Near" solution. (c) (d) show their difference and ratio, respectively.

		SRBY		Total
		Near	Far	
This Study	Near	98	48	146
	Far	15	27	42
Total		113	75	188

Table 4: Number of molecular clouds in Solomon et al. (1987) (SRBY) distinguished by labels “Near” and “Far” in this study and SRBY.

7 Summary

The main results of this study are summarized as follows:

1. We presented high angular resolution and wide ^{12}CO , ^{13}CO , as well as C^{18}O ($J = 1 - 0$) emission data in the 1st quadrant of the Galactic plane obtained with the Nobeyama 45-m radio telescope ($l = 62^\circ - 10^\circ$, $|b| < 1^\circ$).
2. We attempted to construct a Near–Far inference model using a CNN. In this model, we applied the 3D distribution (position–position–velocity) of the ^{12}CO ($J = 1 - 0$) emissions as the main input. The training dataset was made from the HII region catalog of the infrared astronomy satellite WISE. Therefore, we were able to construct a CNN model with a 76% accuracy rate for the training dataset.
3. Using the CLUMPFIND algorithm, we identified approximately 140,000 clouds in the ^{12}CO ($J = 1 - 0$) data. By combining this result with the inference of the CNN model, we obtained the distance to the identified clouds. We discovered that the mass of the molecular clouds with a distance of < 8.15 kpc follows a power-law distribution with an index of approximately -2.3 in the mass range $M > 10^3 M_\odot$. Furthermore, the detailed molecular gas distribution of the Galaxy as seen from the Galactic North pole (face-on-view map) was derived.

Acknowledgments

This study was financially supported by Grants-in-Aid for Scientific Research (KAKENHI) of the Japanese Society for the Promotion of Science (JSPS; grant numbers 17H06740 and JP21H00049) and “Young interdisciplinary collaboration project” in the National Institutes of Natural Sciences (NINS). The authors would like to thank all members of the FUGIN project. Data analysis was performed using Astropy (Astropy Collaboration et al. 2013) and APLpy (Robitaille & Bressert 2012). The authors would also like to thank NASA for providing the FITS data from the WISE Space Telescope. Finally, we wish to express our appreciation to the anonymous reviewer for the insightful comments pertaining to our manuscript.

References

- Anderson, L. D., Bania, T. M., Balsler, D. S., et al. 2014, *ApJS*, 212, 1.
- Astropy Collaboration, Robitaille, T. P., Tollerud, E. J., et al. 2013, *A&A*, 558, A33
- Berry, D. S., Reinhold, K., Jenness, T., Economou, F., 2007, *ASP Conf. Ser.*, 376, 425
- Bom, C. R., Cortesi, A., Lucatelli, G., et al. 2021, *MNRAS*, 507, 1937.
- Dabeer, S., Khan, M. M., & Islam, S. 2019, *Inform. Med. Unlocked*, 16, 100231
- Dame, T. M., Hartmann, D., & Thaddeus, P. 2001, *ApJ*, 547, 792.
- Dempsey, J. T., Thomas, H. S., & Currie, M. J. 2013, *ApJS*, 209, 8.
- Dewangan, L. K., Baug, T., & Ojha, D. K. 2020, *MNRAS*, 496, 1278.
- Dickman, R. L. 1978, *ApJS*, 37, 407
- Frerking, M. A., Langer, W. D., & Wilson, R. W. 1982, *ApJ*, 262, 590
- Fujita, S., Torii, K., Tachihara, K., et al. 2019, *ApJ*, 872, 49.
- Fujita, S., Torii, K., Kuno, N., et al. 2021, *PASJ*, 73, S172.
- Fukui, Y., Tokuda, K., Saigo, K., et al. 2019, *ApJ*, 886, 14.
- Heyer, M., Krawczyk, C., Duval, J., et al. 2009, *ApJ*, 699, 1092.
- Jackson, J. M., Rathborne, J. M., Shah, R. Y., et al. 2006, *ApJS*, 163, 145.
- Kawamura, A., Onishi, T., Yonekura, Y., et al. 1998, *ApJS*, 117, 387.
- Kohno, M., Torii, K., Tachihara, K., et al. 2018, *PASJ*, 70, S50.
- Kohno, M., Tachihara, K., Torii, K., et al. 2021, *PASJ*, 73, S129.
- Kohno, M., Nishimura, A., Fujita, S., et al. 2022, *PASJ*, 74, 24.
- Larson, R. B. 1981, *MNRAS*, 194, 809.
- Leroy, A. K., Schinnerer, E., Hughes, A., et al. 2021, *ApJS*, 257, 43.
- Matsuoka, D., Nakano, M., Sugiyama, D. et al. 2018. *Prog Earth Planet Sci* 5: 80.
- Mège, P., Russeil, D., Zavagno, A., et al. 2021, *A&A*, 646, A74.
- Muraoka, K., Sorai, K., Kuno, N., et al. 2016, *PASJ*, 68, 89.
- Nakanishi, H. & Sofue, Y. 2006, *PASJ*, 58, 847.
- Nishimura, A., Tokuda, K., Kimura, K., et al. 2015, *ApJS*, 216, 18.
- Nishimura, A., Minamidani, T., Umemoto, T., et al., 2018, *PASJ*, 70, S42.
- Pineda, J. E., Rosolowsky, E. W., & Goodman, A. A. 2009, *ApJL*, 699, L134.
- Reid, M. J., Menten, K. M., Brunthaler, A., et al. 2014, *ApJ*, 783, 130.
- Reid, M. J., Dame, T. M., Menten, K. M., et al. 2016, *ApJ*, 823, 77.
- Reid, M. J., Menten, K. M., Brunthaler, A., et al. 2019, *ApJ*, 885, 131.
- Riener, M., Kainulainen, J., Henshaw, J. D., et al. 2020, *A&A*, 640, A72.
- Robitaille, T., & Bressert, E. 2012, *Astrophysics Source Code Library*, ascl:1208.017
- Rosolowsky, E., Keto, E., Matsushita, S., et al. 2007, *ApJ*, 661, 830.
- Rosolowsky, E., Hughes, A., Leroy, A. K., et al. 2021, *MNRAS*, 502, 1218.
- Schmidhuber, J. 2014, *arXiv:1404.7828*
- Schuller, F., Urquhart, J. S., Csengeri, T., et al. 2021, *MNRAS*, 500, 3064.

Shimajiri, Y., Kitamura, Y., Saito, M., et al. 2014, *A&A*, 564, A68.

Solomon, P. M., Rivolo, A. R., Barrett, J., et al. 1987, *ApJ*, 319, 730.

Solomon, P. M. & Rivolo, A. R. 1989, *ApJ*, 339, 919.

Sorai, K., Kuno, N., Muraoka, K., et al. 2019, *PASJ*, 71, S14.

Spitzer, L. 1942, *ApJ*, 95, 329.

Stark, A. A. 1984, *ApJ*, 281, 624.

Tokuda, K., Muraoka, K., Kondo, H., et al. 2020, *ApJ*, 896, 36.

Torii, K., Fujita, S., Matsuo, M., et al. 2018, *PASJ*, 70, S51.

Torii, K., Fujita, S., Nishimura, A., et al. 2019, *PASJ*, 71, S2.

Ueda, S., Fujita, S., Nishimura, A., et al. 2020, *Proc. SPIE*, 11452, 114522L.

Umemoto, T., Minamidani, T., Kuno, N., et al. 2017, *PASJ*, 69, 78.

Villar, V. A., Cranmer, M., Berger, E., et al. 2021, *ApJS*, 255, 24.

Wegg, C., Gerhard, O., & Portail, M. 2015, *MNRAS*, 450, 4050.

Williams, J. P., de Geus, E. J., & Blitz, L. 1994, *ApJ*, 428, 693.

Zhang, B., Moscadelli, L., Sato, M., et al. 2014, *ApJ*, 781, 89.